SCIENCE CHINA
Physics, Mechanics & Astronomy

•Article•

September 2021 Vol. 64 No. 9: 296111
https://doi.org/10.1007/s11433-021-1722-y

Dynamic mechanical relaxation and thermal creep of high-entropy $La_{30}Ce_{30}Ni_{10}Al_{20}Co_{10}$ bulk metallic glass

LangTing Zhang[1], YaJuan Duan[1], Daniel Crespo[2], Eloi Pineda[2], YunJiang Wang[3,4], Jean-Marc Pelletier[5], and JiChao Qiao[1*]

[1] *School of Mechanics, Civil Engineering and Architecture, Northwestern Polytechnical University, Xi'an 710072, China;*
[2] *Department of Physics, Barcelona Research Center in Multiscale Science and Technology, Institute of Energy Technologies, Universitat Politècnica de Catalunya, Barcelona 08019, Spain;*
[3] *State Key Laboratory of Nonlinear Mechanics, Institute of Mechanics, Chinese Academy of Sciences, Beijing 100190, China;*
[4] *School of Engineering Science, University of Chinese Academy of Sciences, Beijing 101408, China;*
[5] *MATEIS, UMR CNRS5510, Université de Lyon, INSA-Lyon, Villeurbanne Cedex F-69621, France*

Received March 2, 2021; accepted May 20, 2021; published online August 3, 2021

Dynamic mechanical relaxation is a fundamental tool to understand the mechanical and physical properties of viscoelastic materials like glasses. Mechanical spectroscopy shows that the high-entropy bulk metallic glass ($La_{30}Ce_{30}Ni_{10}Al_{20}Co_{10}$) exhibits a distinct β-relaxation feature. In the present research, dynamic mechanical analysis and thermal creep were performed using this bulk metallic glass material at a temperature domain around the β relaxation. The components of total strain, including ideal elastic strain, anelastic strain, and viscous-plastic strain, were analyzed based on the model of shear transformation zones (STZs). The stochastic activation of STZ contributes to the anelastic strain. When the temperature or external stress is high enough or the timescale is long enough, the interaction between STZs induces viscous-plastic strain. When all the spectrum of STZs is activated, the quasi-steady-state creep is achieved.

high-entropy bulk metallic glass, mechanical relaxation, creep, recovery process, shear transformation zone, structural heterogeneity

PACS number(s): 61.43.Dq, 62.40.+i, 62.20.Hg

Citation: L. T. Zhang, Y. J. Duan, D. Crespo, E. Pineda, Y. J. Wang, J.-M. Pelletier, and J. C. Qiao, Dynamic mechanical relaxation and thermal creep of high-entropy $La_{30}Ce_{30}Ni_{10}Al_{20}Co_{10}$ bulk metallic glass, Sci. China-Phys. Mech. Astron. **64**, 296111 (2021), https://doi.org/10.1007/s11433-021-1722-y

1 Introduction

Metallic glasses (MGs) and high-entropy alloys (HEAs) have attracted much attention to researchers worldwide over various disciplines. MGs possess unique mechanical and physical properties such as superior compressive/tensile strength, high elastic limit, ultrahigh hardness, and excellent anti-corrosion behavior [1-6]. HEAs are multicomponent alloys containing at least five elements in equiatomic/near-equiatomic concentrations. HEAs exhibit four unique effects, i.e., high configuration entropy, sluggish diffusion, cocktail effect, and severe lattice distortion [7-9]. High-entropy bulk metallic glasses (HE-BMGs) combine both characteristics of MGs and HEAs. Recent literature has reported the specific properties of HE-BMGs, such as excellent glass forming ability [10], ultrahigh compressive strength [11-13], soft magnetic properties [14], and good corrosion resistance [15].

The definition of "defects" in MGs and the correlation between mechanical properties and deformation mechanism

*Corresponding author (email: qjczy@nwpu.edu.cn)

remain open questions, similar to how apparent defects (voids, dislocations, and grain boundaries) play a role in conventional crystalline metals. Mechanical relaxation can be defined as the transition of a system from one thermodynamic state to another, involving energy dissipation due to the application of external mechanical stress. Previous investigations proved that the plastic deformation of MGs is correlated to the rearrangements of local random atomic clusters in soft regions termed shear transformation zones (STZs) [16]. There are two types of plastic deformation in MGs [16,17]. Homogeneous flow, occurring at a low strain rate and develops when shear mediated strain is triggered by activation of STZs [17]. In contrast, inhomogeneous flow, occurring at a high strain rate, occurs when the nucleation and motion of shear banding events are induced by the avalanches of atomic rearrangements in coupled STZs [18-20]. In addition to the mechanistic description, the potential energy landscape (PEL) describes the plastic deformation mechanism of MGs in terms of motion within the configurational space, involving changes of potential energy from one state to another [21,22]. According to the PEL diagram, glassy materials possess two main relaxation processes: secondary β relaxation (also named Johari-Goldstein, JG relaxation) and primary α relaxation [22]. The α relaxation of glassy materials is correlated to the glass transition process, which develops through cooperative, large-scale rearrangement of atoms or molecules. From the perspective of PEL, α relaxation is composed of a series of consecutive β relaxations. The β relaxation, which is attributed to the structural heterogeneity, is relevant to local atomic rearrangement [23-26]. Recent studies proved that the β relaxation is closely associated with the mechanism underlying plastic deformation [27-29]. Significantly, the apparent activation energy of β relaxation E_β in MGs is correlated to the potential energy barriers W_{STZ} of STZs, i.e., $E_\beta \approx W_{STZ}$ [30]. β relaxation is linked to the activation of STZs locally confined in the elastic matrix of MGs, while α relaxation is associated with the percolation of STZs through the elastic matrix [21,31].

In addition, MGs remain in an out-of-equilibrium state. The Gibbs free energy of MGs is higher than that of their crystalline counterparts, and for the ideal metastable liquid when rapidly cooled down from the liquid state. Excess free energy causes spontaneous irreversible structural rearrangements, known as structural relaxation [32]. However, the thermodynamic mechanical relaxation behavior of MG is not fully understood and requires further research [2,3,33]. Notably, the high configuration entropy of HE-BMGs causes a decrease in Gibbs free energy [34]. Hence, HE-BMGs are excellent model systems to probe the evolution of the atomic configuration and time-dependent thermodynamic mechanical relaxation.

Creep behavior is fundamental to understand the plastic deformation in materials [35-37]. The deformation behavior of MGs overlaps the features of elastic solids and viscous fluids. Normally, the strain response of MGs to the applied stressis composed of four components. These diverse components are distinguished by their reliance on time or the degree of recovery upon unloading and are defined as follows:

(1) Ideal elastic strain ε_e, the component of deformation which is instantaneous, linear, and fully recoverable [38].

(2) Anelastic strain (also named backward strain) ε_a, the component of deformation which gives rise to a full recovery with a characteristic time comparable to that of a transitory regime of deformation. Anelastic strain is both directly and indirectly dependent on the rate of loading or heating [39].

(3) Visco-plastic strain ε_{vp} is a non-recoverable and time dependent component [40].

(4) Instantaneous plastic strain ε_p is an instantaneous and non-recoverable component.

Recent literature reports significant advances in understanding the creep process of amorphous materials, including MGs [41-43]. Furthermore, several theoretical models were proposed to describe the mechanical properties of amorphous solids. The classical rheological model, i.e., generalized Kelvin model, is composed of a number of dashpots and springs [44-46]. The flow events in MGs are illustrated in the framework of the PEL [28,47]. It should be emphasized that the creep mechanism in MGs, particularly in HE-BMGs, is still under debate [42,48,49]. In this research, $La_{30}Ce_{30}Ni_{10}Al_{20}Co_{10}$ HE-BMG was selected as a model alloy to study the dynamic mechanical relaxation behavior and the creep mechanism. Both theoretical and experimental studies investigated the correlation among the dynamic mechanical relaxation process, cooperative rearrangement of atoms, and creep dynamics. Mechanical spectroscopy indicates that $La_{30}Ce_{30}Ni_{10}Al_{20}Co_{10}$ HE-BMG exhibits a pronounced slow β relaxation and a distinct α relaxation. Besides, observations of creep and recovery spectra indicate a transition from a three-stage power-law process into a double-stage power-law process.

2 Experimental procedure

2.1 Sample preparation

The master alloys with a nominal atomic composition of $La_{30}Ce_{30}Ni_{10}Al_{20}Co_{10}$ (at%) were prepared by arc-melting pure metals in a Ti-gettered high-purity argon atmosphere. Plates were prepared by a copper mold suction casting technique with a length of ~70 mm, a width of ~10 mm, and a thickness of ~2 mm. The single-roller melt-spinning technique was used to prepare ribbons with a width of ~2 mm and a thickness of ~20 μm.

2.2 Thermal properties

The glass nature of as-cast alloys was confirmed using X-ray

diffraction with Cu Kα radiation using a device (XRD, Bruker AXS Gmbh). The glass transition temperature T_g and the crystallization onset temperature T_x, were measured using a differential scanning calorimeter (DSC, Pekin Elmer, DSC 7) at a heating rate of 10 K/min.

2.3 Mechanical spectroscopy

Dynamic mechanical properties of the model glass were performed using a dynamic mechanical analyzer (DMA, TA instruments Q800) in single-cantilever bending mode. As periodic sinusoidal stress is applied to the materials, the corresponding strain is monitored in the DMA experiments. The dynamic Young's modulus $E^* = E' + iE''$, where E' is the storage modulus, and E'' is the loss modulus, is inferred from σ/ε. The loss factor (also termed internal friction) $\tan\delta = E''/E'$ can also be determined. DMA provides a temperature range from 128 to 873 K and a frequency range from 0.01 to 200 Hz.

2.4 Creep and recovery test

The thermal creep and recovery measurements were performed using a DMA, TA instruments Q800 in tension film mode. The stress level was from 25 to 100 MPa, and temperature ranged from 358 to 403 K.

3 Results and discussion

3.1 Thermal properties of HE-BMG

Figure 1 shows the XRD pattern of $La_{30}Ce_{30}Ni_{10}Al_{20}Co_{10}$ HE-BMG (as-cast state). The broad diffraction peak is a typical feature of amorphous solids. The inset of Figure 1 exhibits the DSC curve of $La_{30}Ce_{30}Ni_{10}Al_{20}Co_{10}$ HE-BMG. The glass transition temperature T_g is 437 K, and the crystallization onset temperature T_x is 492 K. $La_{30}Ce_{30}Ni_{10}Al_{20}Co_{10}$ HE-BMG indicates a broad supercooled liquid region (SLR, $\Delta T = T_x - T_g = 55$ K).

3.2 Dynamic mechanical analysis

The dynamic mechanical relaxation of MGs shows dependence on the driving frequency and temperature [50]. Figure 2(a) presents the dependence of the normalized storage modulus E'/E_u and loss modulus E''/E_u of $La_{30}Ce_{30}Ni_{10}Al_{20}Co_{10}$ HE-BMG on temperature obtained at a driving frequency of 0.5 Hz and a heating rate of 3 K/min. Here, E_u is the storage modulus at ambient temperature. Similar to other La-based and Ce-based MGs, $La_{30}Ce_{30}Ni_{10}Al_{20}Co_{10}$ HE-BMG shows a distinct β relaxation peak. The intensity of β relaxation is approximately 10% of that of α relaxation, according to refs. [51,52]. The results clearly show that the temperature span of the β relaxation is broader than that of α relaxation. Figure 2(b) depicts the normalized loss modulus E''/E''_{max} versus the normalized temperature T/T_α in various HE-BMGs. Here E''_{max} is the maximum value of the loss modulus, and T_α is the peak temperature of α relaxation. $Zr_{35}Hf_{17.5}Ti_{5.5}Al_{12.5}Co_{7.5}Ni_{12}Cu_{10}$ HE-BMG exhibits a moderate secondary relaxation known as "excess wing" whereas

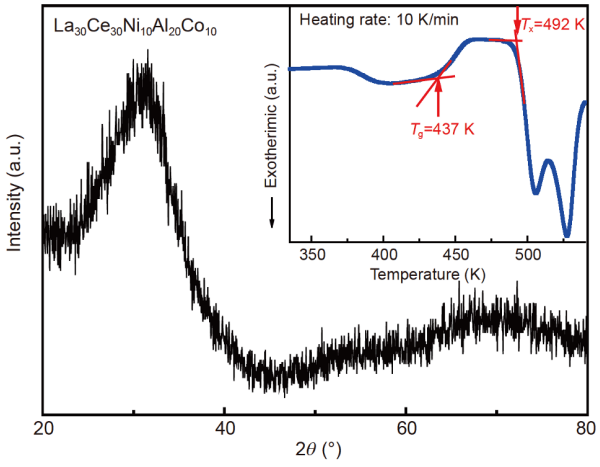

Figure 1 (Color online) XRD pattern of $La_{30}Ce_{30}Ni_{10}Al_{20}Co_{10}$ HE-BMG in as-cast state. No sharp peaks appear, proving the glassy nature of the alloy. The inset exhibits the DSC curve at a heating rate of 10 K/min. The glass transition temperature T_g is 437 K, and the crystallization onset temperature T_x is 492 K.

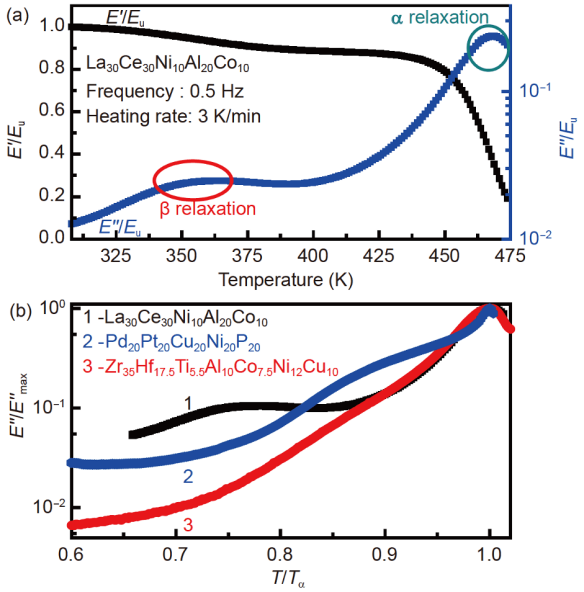

Figure 2 (Color online) (a) Dependence of the normalized storage modulus E'/E_u and loss modulus E''/E_u of the $La_{30}Ce_{30}Ni_{10}Al_{20}Co_{10}$ HE-BMG on temperature obtained at a driving frequency of 0.5 Hz and a heating rate of 3 K/min. Here, E_u is the storage modulus at room temperature; (b) the normalized loss modulus E''/E''_{max} in $La_{30}Ce_{30}Ni_{10}Al_{20}Co_{10}$, $Pd_{20}Pt_{20}Cu_{20}Ni_{20}P_{20}$, and $Zr_{35}Hf_{17.5}Ti_{5.5}Al_{12.5}Co_{7.5}Ni_{12}Cu_{10}$ HE-BMGs as a function of the normalized temperature T/T_α [53]. E''_{max} is the maximum of the loss modulus, and T_α is the temperature of the peak of the main α relaxation.

$Pd_{20}Pt_{20}Cu_{20}Ni_{20}P_{20}$ HE-BMG exhibits a "shoulder" [53]. In this study, $La_{30}Ce_{30}Ni_{10}Al_{20}Co_{10}$ HE-BMG shows a conspicuous β relaxation peak for establishing the correlation between relaxation dynamics and creep mechanism.

To further analyze the nature of the dynamic mechanical relaxation of HE-BMGs, the evolution of the isothermal relaxation spectra, i.e., the loss modulus E''/E_u and scanning the frequency from 0.02 to 16 Hz with temperature intervals of 5 K is shown in Figure 3(a). The spectra of $La_{30}Ce_{30}Ni_{10}Al_{20}Co_{10}$ HE-BMG show a pronounced β relaxation peak within the frequency window at low temperature, while α relaxation appears at the high temperature region. As the isothermal temperature increases, both the β and α relaxation peaks move to a higher frequency.

According to the time-temperature superposition (TTS) principle, the evolution of modulus/compliance of polymers in a broad frequency/time window can be collapsed into a master curve by frequency shifting [54]. Assuming the validity of the TTS principle in MGs, the master curve of loss modulus of $La_{30}Ce_{30}Ni_{10}Al_{20}Co_{10}$ HE-BMG was obtained by a horizontal shift of the isothermal profiles with a temperature shift factor $a_T = \tau(T)/\tau(T_{ref})$, where $\tau(T)$ is the relaxation time at a given testing temperature and $\tau(T_{ref})$ is the relaxation time at a given reference temperature T_{ref}. Figure 3(b) presents the normalized loss modulus as a function of shifted frequency with reference temperature T_{ref} = 358 K, and this temperature was chosen deliberately as the significant creep recovery temperature as discussed below. Consequently, one can compute the dynamic mechanical relaxation at any desired reference temperature using the TTS principle. At high driving frequency, the master curve is primarily dominated by β relaxation, whereas α relaxation peak emerges at low driving frequencies. At temperatures below the glass transition temperature, the correlation between the relaxation time and temperature of glassy materials, including MGs, obeys the Arrhenius equation: $\tau = \tau_0 \exp(E_{glass}/kT)$, where τ_0 is a pre-factor, E_{glass} is the apparent activation energy at glass state and k is the Boltzmann constant. Parallelly, above the glass transition, the relaxation time τ is well described by the Vogel-Fucher-Tammann (VFT) function: $\tau = A\exp(B/(T-T_0))$, where A, B, and T_0 are fitting parameters. In the limited temperature region, the VFT equation can be approximated by the Arrhenius equation: $\tau = \tau'_0 \exp(E_{scl}/kT)$, where τ'_0 is the fitting parameter, and E_{scl} refers to the apparent activation energy in the supercooled liquid (SCL) state. From the perspective of the relaxation time, the shift factor a_T can

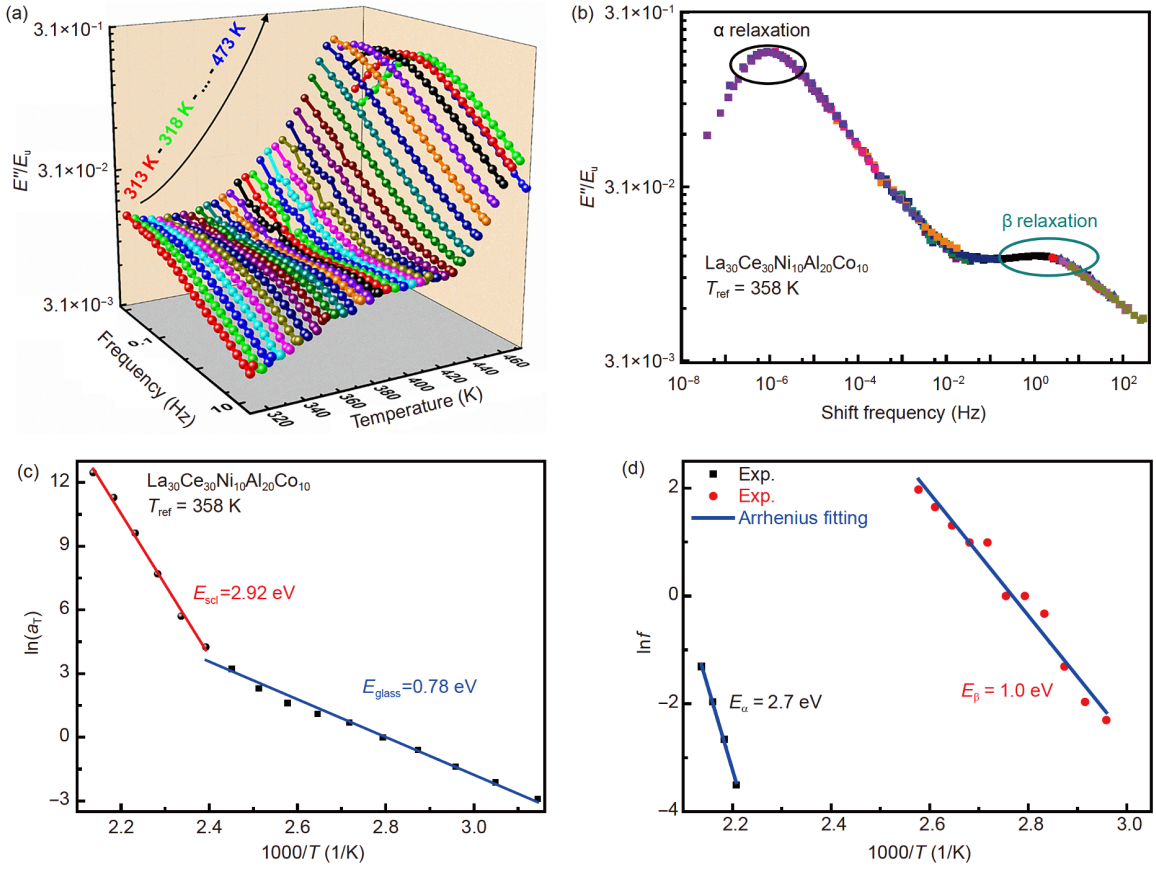

Figure 3 (Color online) (a) Evolution of the normalized loss modulus E''/E_u as a function of frequency at different temperatures of $La_{30}Ce_{30}Ni_{10}Al_{20}Co_{10}$ HE-BMG; (b) master curve of the normalized loss modulus E''/E_u is based on the TTS principle; the reference temperature is T_{ref} = 358 K; (c) temperature dependence of the shift factor for DMA; the solid lines represent fits to Arrhenius equations; (d) the evolution of the peak values of α relaxation and β relaxation as a function of reciprocal temperature. The solid lines denote Arrhenius fits. The apparent activation energies of relaxation are presented.

be well described as [55]:

$$a_{\mathrm{T}}=\begin{cases}\exp\left[\dfrac{E_{\mathrm{glass}}}{k}\left(\dfrac{1}{T}-\dfrac{1}{T_{\mathrm{ref}}}\right)\right], & T<T_{\mathrm{g}},\\ \exp\left[\dfrac{E_{\mathrm{scl}}}{k}\left(\dfrac{1}{T}-\dfrac{1}{T_{\mathrm{ref}}}\right)\right], & T\geq T_{\mathrm{g}}.\end{cases} \tag{1}$$

Figure 3(c) presents a plot of the shift factor a_{T} as a function of the reciprocal of temperature for T_{ref} = 358 K. The result explicitly shows a perfect fitting of the evolution of the shift factor a_{T} on temperature. In the present work, the master curve was successfully generated based on the TTS principle. Besides, the correlation between the peak temperature of the β relaxation and the driving frequency of glassy materials also obeys the Arrhenius equation: $f=f_0\exp(E_\beta/kT)$, where f_0 is a pre-factor and E_β is the apparent activation energy of the β relaxation. Figure 3(d) depicts the logarithm of the driving frequency versus the reciprocal of the peak temperature of α and β relaxations. The slope of the fitted line allows to compute the apparent activation energies of the β and α relaxations, i.e., E_β = 1.0 eV and E_α= 2.7 eV, respectively. These values are very similar to those obtained for E_{glass} and E_{scl}, respectively. Remarkably, $E_\beta = 26.4RT_{\mathrm{g}}$ is consistent with the empirical ratio for the activation energy of the β relaxation of typical MGs [56]. The activation energy obtained from the shift factor is close to that computed from the driving frequency, demonstrating that the TTS principle is suitable in HE-BMGs and that the activation energies controlling both α and β relaxation in the glass state computed by alternative methods are very similar.

3.3 Creep tests

The tensile creep measurements of ribbons submitted to applied stress of 50 MPa in a wide temperature region (from 358 to 403 K) are illustrated in Figure 4(a), and the strain is obtained by subtracting the elastic strain from the total strain. At a given temperature, the strain increases with time. Two regions are observed: in stage I, the primary creep, where the strain rate is decreasing with increasing strain; in stage II, the quasi-steady-state creep, where an approximately linear strain increases with time, is observed. In stage II, the phenomenological quasi-steady-state creep rate $\dot{\varepsilon}_{\mathrm{qss}}$ shows a strong temperature dependence. Previous investigations reported that creep strain rate could be used to systematically study the time-dependent deformation behavior of viscoelastic materials [57,58]. In addition, the dependence of $\dot{\varepsilon}_{\mathrm{qss}}$ on both temperature and applied stress can be described by the Arrhenius equation:

$$\dot{\varepsilon}_{\mathrm{qss}}=A_0\exp\left(\frac{E_0-\dfrac{\sigma}{\sqrt{3}}V}{kT}\right), \tag{2}$$

where A_0 is a constant; σ is the applied stress; E_0 is the unbiased creep activation energy, which is a vital parameter corresponding to the correlation between deformation units and creep mechanism; V denotes the apparent activation volume. At constant stress, eq. (2) becomes $\dot{\varepsilon}_{\mathrm{qss}}=A_0\exp\left(\dfrac{E_{\mathrm{creep}}}{kT}\right)$, where E_{creep} is the apparent activation energy of creep. Figure 4(b) presents the evolution of logarithm of $\dot{\varepsilon}_{\mathrm{qss}}$ versus the reciprocal of temperature. The activation energy obtained from the fitting is E_{creep} = 0.40 eV, which is significantly smaller than the activation energy of β relaxation. Though the relaxation dynamics are strongly dependent on the quenching rate of the sample preparation, i.e., at cooling rates of ~10^3 K/s (for bulk) and ~10^5 K/s (for ribbon), the obvious difference indicates that mechanical work reduces the activation energy during creep deformation [59]. A creep master curve can be obtained over a wide time window by considering the reference temperature T_{ref} = 358 K, represented in the logarithmic shift time scale in Figure 4(c). In the viscoelastic regime, the relationship between the elastic modulus $E(t)$ and creep compliance $J(t)$ in the Laplace form obeys $t=\int_0^t E(s)J(t-s)\mathrm{d}s$, probing the correlation between DMA and creep. Figure 4(d) presents the best fitting of the shift factor a_{T}, obtained from the creep master curve, to the Arrhenius equation. The apparent activation energy of deformation units U_{c} is obtained as 1.81 eV.

Previous literature reported that structural heterogeneity in MGs was verified by experiments, theoretical analysis, and simulations [2,3,44,60-62], indicating a broad distribution of energy barriers E_{app} of deformation units. The creep curves in the framework of activation energy spectrum (AES) can be used to determine the activated deformation units [63]:

$$\Delta\varepsilon(t)=\int_0^\infty p\left(E_{\mathrm{app}}\right)\theta\left(E_{\mathrm{app}},T,t\right)\mathrm{d}E_{\mathrm{app}}, \tag{3}$$

where $p(E_{\mathrm{app}})$ is the property change ranging from E_{app} + $\mathrm{d}E_{\mathrm{app}}$; $\theta(E_{\mathrm{app}}, T, t)$ is the aging function [63]:

$$\theta\left(E_{\mathrm{app}},T,t\right)=1-\exp\left[-\nu_{\mathrm{D}}t\exp\left(\frac{-E_{\mathrm{app}}}{kT}\right)\right]. \tag{4}$$

Based on the step-like approximation [64,65]:

$$p\left(E_{\mathrm{app}}\right)=\frac{-1}{kT}\frac{\mathrm{d}\varepsilon}{\mathrm{d}\ln t}, \tag{5}$$

$$E_{\mathrm{app}}=kT\ln(\nu t), \tag{6}$$

where ν_{D} is Debye frequency and the evolution of AES with temperature is shown in Figure 5(a). Here, only the deformation units in which $E_{\mathrm{app}} < E_{\mathrm{c}}$ (E_{c} is the critical energy barrier) contribute to the creep process. By increasing the temperature, the apparent activation energy spectra shift toward higher energies. At the same time, the critical energy

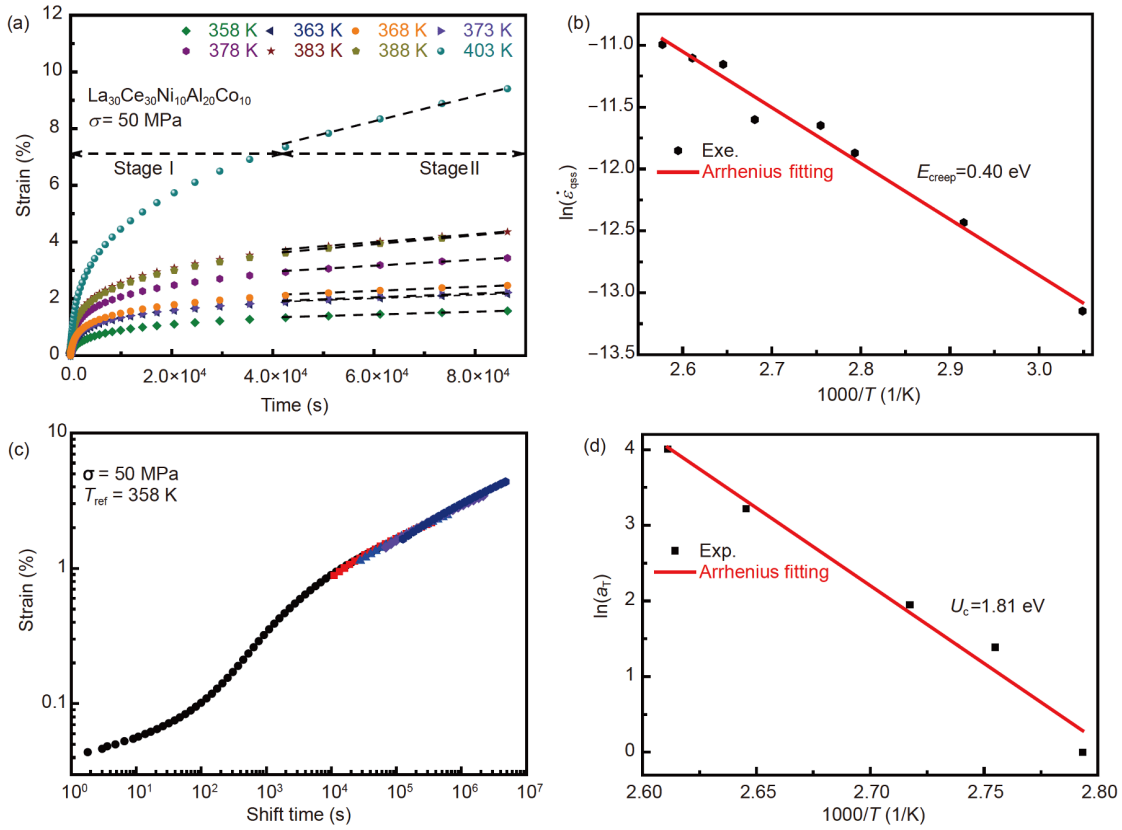

Figure 4 (Color online) (a) Tensile creep curves of $La_{30}Ce_{30}Ni_{10}Al_{20}Co_{10}$ HE-BMG at various temperatures from 358 to 403 K (T_g = 437 K) at tensile stress σ = 50 MPa; (b) reciprocal temperature dependence of the logarithmic quasi-steady-state creep rate $\dot{\varepsilon}_{qss}$; (c) master curve of strains based on the TTS principle; the reference temperature T_{ref} = 358 K; (d) temperature dependence of the shift factor for creep. The solid line is an Arrhenius fit.

barrier E_c also increases with temperature (Figure 5(b)). The relative concentration of the deformation units, the integral of the creep processes from E_0 to E_c, increases by increasing the temperature, confirming that more deformation units can be activated at elevated temperatures (Figure 5(c)). Figure 5(d) depicts the full width at half maximum (FWMH) obtained from AES fitted by Gaussian stochastic distribution upon temperature. The parameter FWMH increases from 0.11 to 0.22 with an increase of temperature of $La_{30}Ce_{30}Ni_{10}Al_{20}Co_{10}$ HE-BMG, suggesting that the distribution of energy barrier of deformation units becomes more dispersive. Several theoretical models are proposed to describe the "defects" of MGs, such as the free volume model [17], flow units model [3], liquid-like sites [66], quasi-point defect model [67], and interstitialcy model [68]. At low temperatures, the glassy body consists of the elastic matrix and flow units. The increase of the temperature drives a conversion from the elastic matrix into flow units, which increases the number of flow units contributing to the relaxation process. As a result, the metallic glass system exhibits greater heterogeneity at a higher temperature. It shows that the increased rate of FWMH is higher as the temperature increases, indicating that high temperature accelerates the extension of the relaxation.

However, the expected behavior of the FWHM increases as temperature rises, with a moderate increase between 358 and 388 K, followed by a large increase at 403 K. A possible explanation of the observed increase of dynamical heterogeneity is the generation of a two-phase glass, in a process similar to spinodal decomposition already found in crystalline HEAs [69].

As mentioned above, the mechanism underlying the strain rate is still unclear; thus, we focused on the strain rate during the creep experiments. Figure 6(a) exhibits the plot of $\log(\dot{\varepsilon})$ vs. $\log(t)$ in the creep measurement performed at 403 K under applied stress of 50 MPa, showing a two-stage power-law. The intersection of the two lines defines as crossover time τ_c = 310 s. This crossover between two relaxations has also been reported in dielectric materials [70] and stress relaxation tests in MGs [71-74]. According to molecular dynamics simulations, the power-law creep in glassy systems is correlated to the percolation dynamics of soft regions [75]. The delayed appearance of the second relaxation in the form of power law illustrates that the frozen deformation units can be activated after sufficient incubation time. The power exponents are obtained with values m = 0.36 for the fast relaxation and q = 0.71 for the slow relaxation. The change of the power exponent is induced by the transition between

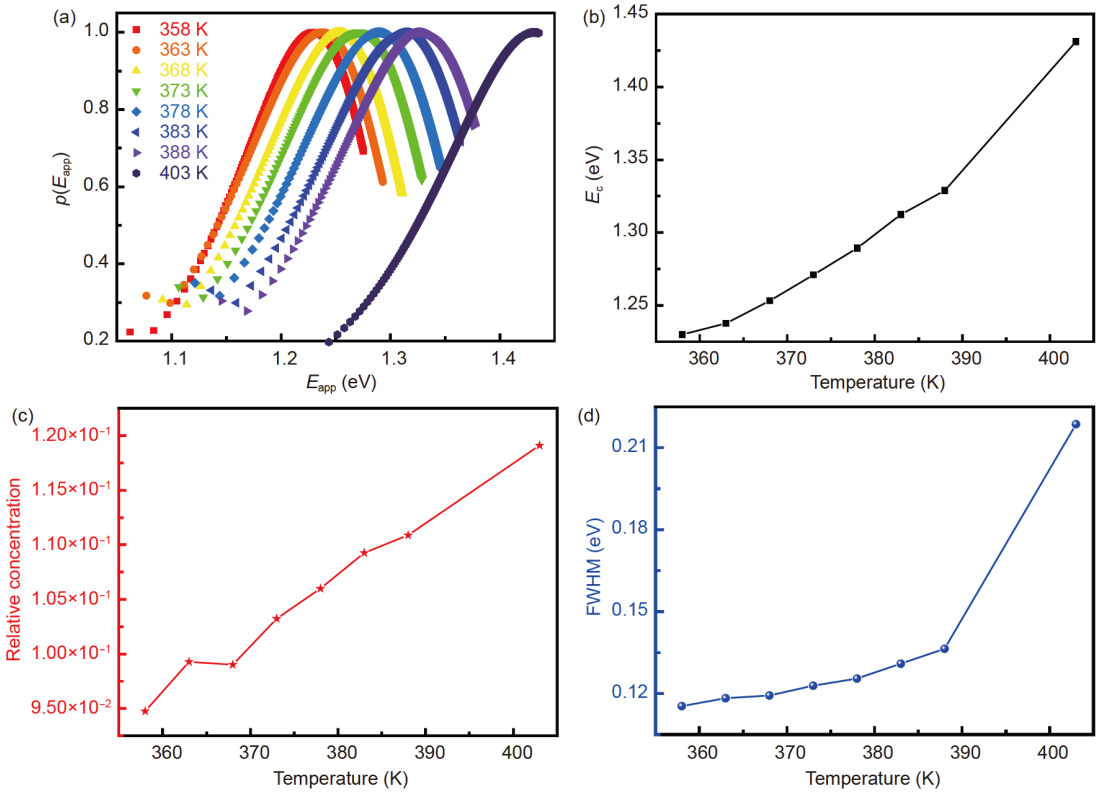

Figure 5 (Color online) (a) The evolution of the normalized activation energy spectra $p(E_{app})$ as a function of temperature in $La_{30}Ce_{30}Ni_{10}Al_{20}Co_{10}$ HE-BMG. Temperature dependence of the critical energy barrier E_c (b), the relative concentration (c), and the full width at half maximum (FWMH) (d) of activation energy spectra for $La_{30}Ce_{30}Ni_{10}Al_{20}Co_{10}$ HE-BMG.

different deformation patterns of STZs. Notably, the crossover from a fast relaxation to a slow relaxation is a characteristic nature of MGs, and the understanding of such a crossover in MGs is unambiguously significant. Figure 6(b) depicts the evolution of strain rate over time at different temperatures showing that the higher the temperature, the greater the creep strain rate. Interestingly, a three-stage power-law dependence emerges at the low temperature region. Figure 6(c) shows $\log(\dot{\varepsilon})$ vs. $\log(t)$ at 358 K. Here, we redefined the exponents of the three-stage power-law processes as a, b, and c with τ_{c1} and τ_{c2}, the successive crossover times. The computed power exponents become a=0.55 for the first relaxation, b=0.25 for the second relaxation, and c= 0.87 for the third relaxation, with crossover times τ_{c1}= 32 s and τ_{c2} = 740 s. In addition, Figure 6(d) shows the log-log plot of the strain rate against time of various MGs, confirming that the three-stage power-law creep is a universal characteristic for MGs. All the parameters, i.e., power exponents and crossover times, are shown in Figure 7(a) and (b). The following observation was made:

(1) The power exponent a decreases by increasing the temperature whereas exponent b increases. A lower value of a reflects that the decay of the strain rate is slower, and the quasi-stable state is reached faster. In this research, the value of $a = b$ at a critical temperature of 390 K.

(2) The power exponent c decreases as temperature increases.

(3) Both the crossover times τ_{c1} and τ_{c2} decrease as the temperature increases. The transition between relaxations is accelerated by a rise in temperature, which increases the atomic mobility of the metallic glass. As the temperature approaches 390 K, the value of τ_{c1} is approximately zero, reflecting the coupling of relaxations.

Stress jump tests at given temperatures were also performed to study the rheological behavior of the glassy materials. Figure 8(a) exhibits creep curves of $La_{30}Ce_{30}Ni_{10}Al_{20}Co_{10}$ HE-BMG in the ranges from 358 to 388 K at different applied stresses. The experimental results prove that the $\dot{\varepsilon}_{qss}$ increases with the increase of the applied stress or testing temperature. Stress exponent n, which represents the correlation between $\dot{\varepsilon}_{qss}$ and applied stress at a given temperature, is expressed as $n = \frac{\partial \ln \sigma}{\partial \ln \dot{\varepsilon}_{qss}}\Big|_T$. Figure 8(b) shows the logarithm of applied stress vs. logarithm of $\dot{\varepsilon}_{qss}$. The value of n can be readily calculated from the slope as 1.40, 1.43, and 1.44 for T = 358, 373, and 388 K, respectively. The dependence of the activation volume on both applied stress and temperature can be expressed by the general partial differential of eq. (2) as follows [76]:

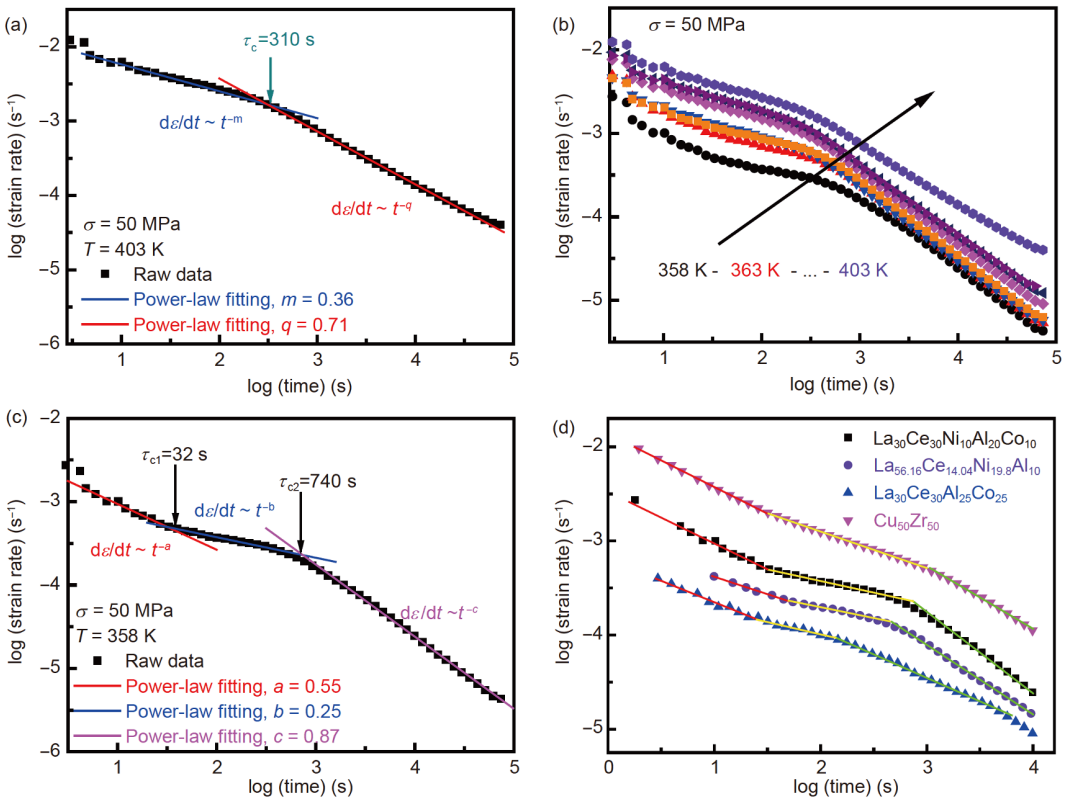

Figure 6 (Color online) (a) Log-log plot of the strain rate against time at 403 K (T_g = 437 K). Two regions following a distinct power-law decay, correlating with the fast and slow relaxation modes, are separated. The power-law exponents with m = 0.36 and q = 0.71. A crossover time τ_c = 310 s is obtained. (b) The evolution of the power-law decay at different temperatures. As temperature decreases, the third part of distinct power-law decay emerges. (c) Log-log plot of the strain rate against time at 358 K. Three distinct power-law decays with corresponding power-law exponents a = 0.55, b = 0.25, and c = 0.87 are obtained. Crossover times are in this case τ_{c1} = 32 s and τ_{c2} = 740 s. (d) Log-log plot of the strain rate against the time of various MGs.

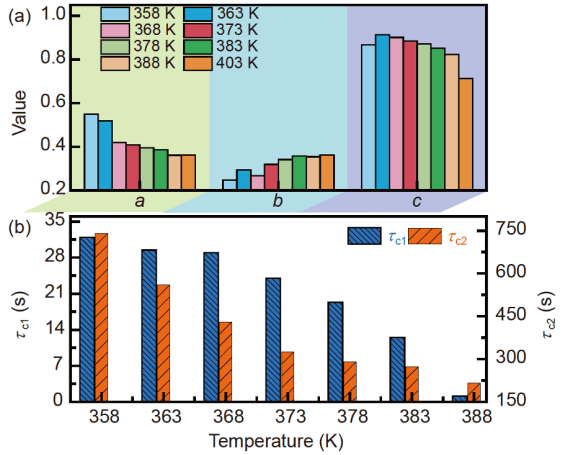

Figure 7 (Color online) Temperature dependence of the power-law exponents a, b, and c (a) and the crossover times τ_{c1} and τ_{c2} (b).

$$\frac{V}{\sqrt{3}} = -kT\left(\frac{\partial \ln A_0}{\partial \sigma} - \frac{1}{n\sigma}\right) = \frac{\sqrt{3}kT}{n\sigma}. \quad (7)$$

Figure 9 illustrates the correlations among the activation volume, applied stress, and temperature. The results show that the smallest activation volume comes into sight on the 358 K and 25 MPa whereas the largest activation volume appears with the temperature of 388 K and the applied stress of 100 MPa. As a consequence, $\dot{\varepsilon}_{qss}$ increases with the increase of activation volume.

3.4 Recovery experiments

Understanding the physical origin and mechanical mechanism underlying the power-law relaxation observed in $La_{30}Ce_{30}Ni_{10}Al_{20}Co_{10}$ HE-BMG is critical. Creep and recovery experiments provide new insight into the interplay between macroscopic inelastic behavior and microscopic deformation units. As illustrated above, the creep at 358 K shows a significant three power-law creep. This temperature was selected to study the creep recovery, and the reference temperature of the master curves of loss modulus (DMA) and strain (creep) was also chosen to be 358 K. We performed experiments in which 50 MPa was loaded to the system, crept for a fixed time, and then unloaded it by releasing the stress back down to zero. The inset of Figure 10 shows the representative strain recovery after the operation of creep for different times t_i, i = 1, 2, 3. It is convenient to mention that t_1 = 0.3 min is smaller than the first crossover time; t_2 = 3 min falls between the first and second crossovers; t_3 = 30 min is

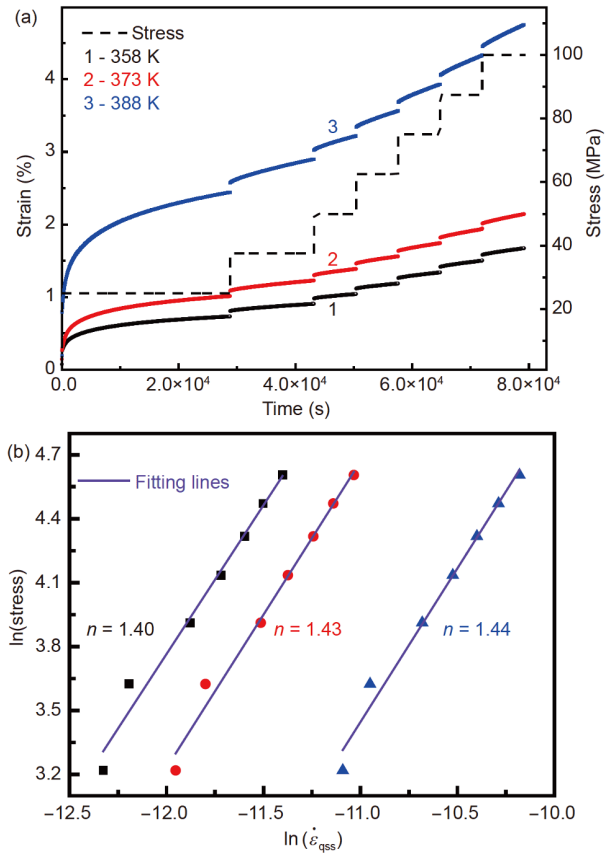

Figure 8 (Color online) (a) Stress jump creep experiment for $La_{30}Ce_{30}Ni_{10}Al_{20}Co_{10}$ HE-BMG at various isothermal temperatures, i.e., 358, 373, and 388 K, respectively; (b) log-log plot of the quasi-steady-state creep rate as a function of the applied creep stress. The solid lines are linear fittings where slope is the stress exponent, n. The value of n is fitted as 1.40, 1.43, and 1.44, respectively.

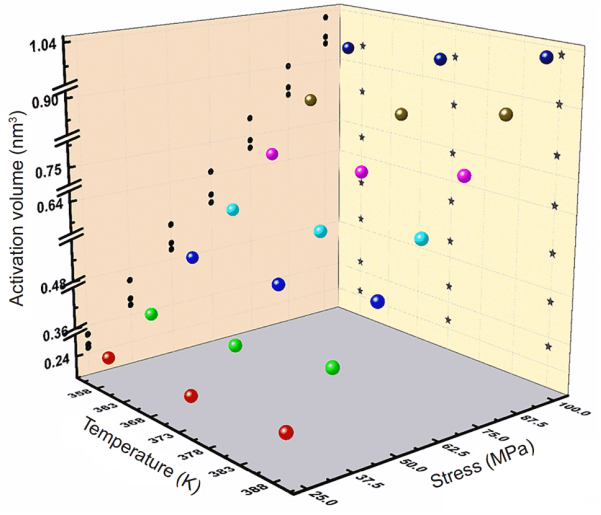

Figure 9 (Color online) The evolution of activation volume as a function of temperature and applied stress. The circles and stars are the projection onto the planes of the coordinate axis.

larger than the second crossover time. The anelastic component is shown to contribute throughout the creep test (referred to the inset), although constant strain-rate steady-state flow is not fully established until the decay of anelastic transient. The anelastic component was obtained by subtracting the ideal elastic contribution to the recovery strain. However, the time-dependent, transient nature of the flow is evident, and true anelastic behavior requires complete recoverability.

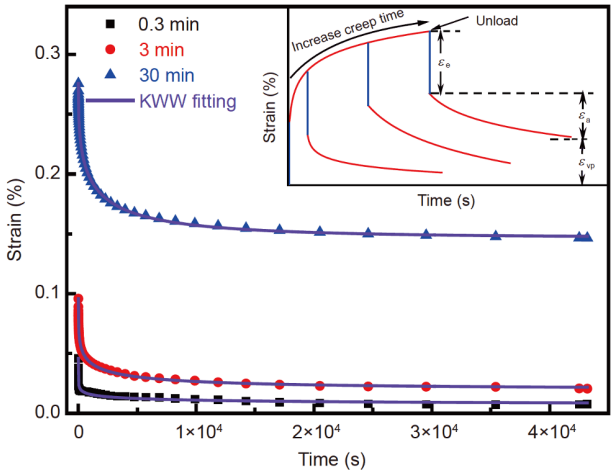

Figure 10 (Color online) Strain versus the time after different creep times 0.3, 3, and 30 min at 358 K. The solid curves are the results of phenomenological KWW fittings. The inset shows the schematic plot of strain along the creep and recovery tests. Three components, i.e., elastic strain ε_e, anelastic strain ε_a, and viscous-plastic strain ε_{vp}, are separated.

The strain recovery curves were fitted by a phenomenological Kohlrausch-Williams-Watts (KWW) function, which is an empirical stretched exponential function and can describe the relaxation spectrum of anelastic deformation of glassy systems [77,78], i.e.,

$$\varepsilon(t=0)-\varepsilon(t)=\varepsilon_0\left[1-\exp\left(-\frac{t}{\tau_{\mathrm{KWW}}}\right)^{\beta_{\mathrm{KWW}}}\right], \tag{8}$$

where ε_0 is the maximum magnitude of the transient creep process; τ_{KWW} is the characteristic time of the recovery process; β_{KWW} is the stretched parameter closely correlated to the structural heterogeneity of glass [61,78,79]. Figure 10 shows the strain recovery curves after different creep times 0.3, 3, and 30 min. The solid curves are the results of the phenomenological KWW fittings. The results prove that the viscous-plastic or permanent deformation increases with the increase of the creep time. The residual strain is almost negligible after the applied load is removed for an applied stress of 50 MPa, creeping for 0.3 min. For creeping of 3 min, the residual strain reaches 0.02% after recovery for 12 h. Besides, the residual strain reaches 0.14% for creeping of 30 min. This permanent deformation and irreversible atomic rearrangement are attributed to the operation of the above three relaxation modes. In addition, the residual strain, which is closely correlated to the creep mechanism of HE-BMGs, is not proportional to creep time. With the increase of

the creep time, the parameter β_{KWW} increases from 0.17 to 0.42, and τ_{KWW} increases from 161 to 1120 s. The parameter β_{KWW} is related to the width of the distribution of relaxation times, and a larger β_{KWW} indicates less dynamic heterogeneity of MGs. As the creep time increases, more deformation units are activated, ascribing to the relaxation process. The increase of β_{KWW} indicates a decrease in the dynamic heterogeneity as the creep time increases. The characteristic time τ_{KWW} increases with the increase of creep time, indicating that the inelastic strain recovery would reach a stable state in a longer time scale.

We now review these findings in the framework of STZs. The structure of glasses can be considered isotropic on a scale larger than that of the deformation units. Furthermore, it is generally accepted that the total number of potential deformation units is constant. While the stress is low enough, the potential deformation units drift in "dilute solution" and are spatially isolated [80]. In the first stage, the activation of STZs is entirely random, and they almost do not interact. Argon et al. [81] reported that the deformation units possess certain configuration memory ability, and they store internal back stress under external stress. If the applied stress is low or the creep time is limited, the deformation is accommodated by single units surrounded by an elastic matrix. The internal back stress dominates the mechanical response after removing the applied stress, and the deformed regions drive the glass completely back to the initial configuration. This microscopic rearrangement is responsible for the reversible anelastic strain ε_a. The activation energy spectra in Figure 5(a) follow a Gaussian distribution, act as a visual window to study the creep mechanism. The AES shifts to a higher temperature region whereas the creep process climbs along the available spectrum, indicating that more deformation units can be activated with increased time and temperature. At relatively high temperatures or after long loading times, residual potential deformation units are transformed into a sheared state. Notably, an activated STZ could operate surrounding STZs [82]. While the activation of an isolated STZ occurs within an elastic glass matrix confinement, both temperature and stress field arouse a redistribution of internal stress and strain around the STZ region. Furthermore, it is expectable that the probability of interaction between the contiguous activated deformation units increases with the temperature or loading time. As a consequence, this interplay introduces a redistribution of free volume and/or internal back stress, leading to a progressive loss of the initial deformation topology. If temperature is high enough, the initial deformation topology would be instantaneously lost on the application of external stress. The instantaneous strain of glassy systems is composed of ideal elastic strain ε_e and instantaneous plastic strain ε_p. With the release of external stress, the interacting activated deformation units will not revert to their undeformed topology, accommodating the permanent component of the total deformation.

During the creep process, the macroscopic inelastic strain is being accumulated as local irreversible deformation via the interaction between contiguous deformation units. After a transient time, the deformation units reach the external stress, and the MGs attain an asymptotic saturated level. Deformation units become spatially correlated, forming contiguous quasi-planar clusters throughout the MGs, resulting in a quasi-steady-state creep [83]. Researchers showed that the annihilation of free volume triggers strain hardening whereas its regeneration introduces plastic flow softening [84,85]. Hence, the quasi-steady-state creep in the homogeneous deformation regime results from a dynamic balance between the annihilation of free volume and its regeneration.

4 Conclusion

In summary, the dynamic mechanical relaxation behavior of $La_{30}Ce_{30}Ni_{10}Al_{20}Co_{10}$ HE-BMG was investigated by mechanical spectroscopy. Both isochronal and isothermal spectra demonstrate that $La_{30}Ce_{30}Ni_{10}Al_{20}Co_{10}$ HE-BMG exhibits two relaxation processes, namely main α relaxation and slow β relaxation. The creep process was quantified and discussed; it ascends along the activation energy spectra, indicating that deformation units are activated by loading time and temperature. By decreasing the temperature, a three-stage power-law creep process emerges, and the underlying mechanism is described in the framework of the STZs. The stochastic activation of independent STZs causes the anelastic strain, and the interplay between STZs induces the visco-plastic strain. Finally, the quasi-steady-state creep is achieved when the number of activated STZs is saturated.

This work was supported by the National Natural Science Foundation of China (Grant No. 51971178), and the Natural Science Basic Research Plan for Distinguished Young Scholars in Shaanxi Province (Grant No. 2021JC-12). E. Pineda and D. Crespo acknowledge financial support from MICINN (Grant No. FIS2017-82625-P), and Generalitat de Catalunya (Grant No. 2017SGR0042). LangTing Zhang is sponsored by the Innovation Foundation for Doctor Dissertation of Northwestern Polytechnical University (Grant No. CX2021015). YunJiang Wang is financially supported by the National Natural Science Foundation of China (Grant No. 12072344).

1 W. L. Johnson, Prog. Mater. Sci. **30**, 81 (1986).
2 J. C. Qiao, Q. Wang, J. M. Pelletier, H. Kato, R. Casalini, D. Crespo, E. Pineda, Y. Yao, and Y. Yang, Prog. Mater. Sci. **104**, 250 (2019).
3 W. H. Wang, Prog. Mater. Sci. **106**, 100561 (2019).
4 L. C. Zhang, Z. Jia, F. Lyu, S. X. Liang, and J. Lu, Prog. Mater. Sci. **105**, 100576 (2019).
5 A. Inoue, W. Zhang, T. Zhang, and K. Kurosaka, Acta Mater. **49**, 2645 (2001).
6 J. Dong, Y. Huan, B. Huang, J. Yi, Y. H. Liu, B. A. Sun, W. H. Wang, and H. Y. Bai, Innovation **2**, 100106 (2021).
7 Y. Zhang, T. T. Zuo, Z. Tang, M. C. Gao, K. A. Dahmen, P. K. Liaw, and Z. P. Lu, Prog. Mater. Sci. **61**, 1 (2014).
8 P. Sathiyamoorthi, and H. S. Kim, Prog. Mater. Sci. doi: 10.1016/j.

pmatsci.2020.100709.
9 Y. F. Ye, Q. Wang, J. Lu, C. T. Liu, and Y. Yang, Mater. Today **19**, 349 (2016).
10 A. Takeuchi, N. Chen, T. Wada, Y. Yokoyama, H. Kato, A. Inoue, and J. W. Yeh, Intermetallics **19**, 1546 (2011).
11 Y. Tong, J. C. Qiao, C. Zhang, J. M. Pelletier, and Y. Yao, J. Non-Cryst. Solids **452**, 57 (2016).
12 H. Y. Ding, and K. F. Yao, J. Non-Cryst. Solids **364**, 9 (2013).
13 S. F. Zhao, G. N. Yang, H. Y. Ding, and K. F. Yao, Intermetallics **61**, 47 (2015).
14 T. Qi, Y. Li, A. Takeuchi, G. Xie, H. Miao, and W. Zhang, Intermetallics **66**, 8 (2015).
15 H. F. Li, X. H. Xie, K. Zhao, Y. B. Wang, Y. F. Zheng, W. H. Wang, and L. Qin, Acta Biomater. **9**, 8561 (2013).
16 A. S. Argon, Acta Metall. **27**, 47 (1979).
17 F. Spaepen, Scr. Mater. **54**, 363 (2006).
18 J. Antonaglia, W. J. Wright, X. Gu, R. R. Byer, T. C. Hufnagel, M. LeBlanc, J. T. Uhl, and K. A. Dahmen, Phys. Rev. Lett. **112**, 155501 (2014), arXiv: 1312.6179.
19 J. Antonaglia, X. Xie, G. Schwarz, M. Wraith, J. Qiao, Y. Zhang, P. K. Liaw, J. T. Uhl, and K. A. Dahmen, Sci. Rep. **4**, 4382 (2014).
20 A. L. Greer, Y. Q. Cheng, and E. Ma, Mater. Sci. Eng.-R-Rep. **74**, 71 (2013).
21 J. S. Harmon, M. D. Demetriou, W. L. Johnson, and K. Samwer, Phys. Rev. Lett. **99**, 135502 (2007).
22 P. G. Debenedetti, and F. H. Stillinger, Nature **410**, 259 (6825).
23 F. Zhu, H. K. Nguyen, S. X. Song, D. P. B. Aji, A. Hirata, H. Wang, K. Nakajima, and M. W. Chen, Nat. Commun. **7**, 11516 (2016).
24 Y. H. Liu, G. Wang, R. J. Wang, D. Q. Zhao, M. X. Pan, and W. H. Wang, Science **315**, 1385 (2007).
25 H. B. Yu, R. Richert, and K. Samwer, Sci. Adv. **3**, e1701577 (2017).
26 Q. Yang, S. X. Peng, Z. Wang, and H. B. Yu, Natl. Sci. Rev. **7**, 1896 (2020).
27 H. B. Yu, X. Shen, Z. Wang, L. Gu, W. H. Wang, and H. Y. Bai, Phys. Rev. Lett. **108**, 015504 (2012).
28 B. Cui, Z. Evenson, B. Fan, M. Z. Li, W. H. Wang, and A. Zaccone, Phys. Rev. B **98**, 144201 (2018), arXiv: 1810.02967.
29 Q. L. Bi, Y. J. Lü, and W. H. Wang, Phys. Rev. Lett. **120**, 155501 (2018).
30 H. B. Yu, W. H. Wang, H. Y. Bai, Y. Wu, and M. W. Chen, Phys. Rev. B **81**, 220201 (2010).
31 W. L. Johnson, and K. Samwer, Phys. Rev. Lett. **95**, 195501 (2005).
32 S. S. Tsao, and F. Spaepen, Acta Metall. **33**, 881 (1985).
33 Q. Wang, J. J. Liu, Y. F. Ye, T. T. Liu, S. Wang, C. T. Liu, J. Lu, and Y. Yang, Mater. Today **20**, 293 (2017).
34 P. Gong, S. Zhao, H. Ding, K. Yao, and X. Wang, J. Mater. Res. **30**, 2772 (2015).
35 O. P. Bobrov, K. Csach, S. V. Khonik, K. Kitagawa, S. A. Lyakhov, M. Y. Yazvitsky, and V. A. Khonik, Scr. Mater. **56**, 29 (2007).
36 D. Caillard, and J. L. Martin, *Thermally Activated Mechanisms in Crystal Plasticity* (Elsevier, Oxford, 2003).
37 I. W. Chen, and A. S. Argon, Acta Metall. **27**, 785 (1979).
38 H. S. Chen, Rep. Prog. Phys. **43**, 353 (1980).
39 R. Maddin, and T. Masumoto, Mater. Sci. Eng. **9**, 153 (1972).
40 A. I. Taub, and F. Spaepen, J. Mater. Sci. **16**, 3087 (1981).
41 Z. R. Xu, D. S. Yang, J. C. Qiao, J. M. Pelletier, D. Crespo, E. Pineda, and Y. J. Wang, Intermetallics **125**, 106922 (2020).
42 Y. Tong, W. Dmowski, H. Bei, Y. Yokoyama, and T. Egami, Acta Mater. **148**, 384 (2018).
43 J. Wu, Z. Zhou, H. Yang, L. Wang, X. Liang, J. Pi, and J. Yi, J. Alloys Compd. **827**, 154298 (2020).
44 J. C. Ye, J. Lu, C. T. Liu, Q. Wang, and Y. Yang, Nat. Mater. **9**, 619 (2010).
45 A. Castellero, B. Moser, D. I. Uhlenhaut, F. H. D. Torre, and J. F. Löffler, Acta Mater. **56**, 3777 (2008).
46 A. Concustell, J. Sort, A. L. Greer, and M. D. Baró, Appl. Phys. Lett. **88**, 171911 (2006).
47 W. H. Wang, J. Appl. Phys. **110**, 053521 (2011).
48 M. E. Kassner, K. Smith, and V. Eliasson, J. Mater. Res. Tech. **4**, 100 (2015).
49 D. Deng, F. Zheng, Y. Xu, G. Qi, and A. S. Argon, Acta Metall. Mater. **41**, 1089 (1993).
50 K. P. Menard, *Dynamic Mechanical Analysis: A Practical Introduction* (CRC Press, Boca Raton, Florida, 2008), pp. 1–25.
51 Q. Wang, S. T. Zhang, Y. Yang, Y. D. Dong, C. T. Liu, and J. Lu, Nat. Commun. **6**, 7876 (2015).
52 B. Huang, C. C. Yuan, Z. Q. Wang, Y. Tong, Q. Wang, J. Yi, G. Wang, Q. F. He, C. H. Shek, and Y. Yang, Acta Mater. **196**, 88 (2020).
53 L. T. Zhang, Y. J. Duan, T. Wada, H. Kato, J. M. Pelletier, D. Crespo, E. Pineda, and J. C. Qiao, J. Mater. Sci. Tech. **83**, 248 (2021).
54 N. M. Alves, J. F. Mano, J. L. Gómez Ribelles, and J. A. Gómez Tejedor, Polymer **45**, 1007 (2004).
55 H. T. Jeong, J. M. Park, W. T. Kim, and D. H. Kim, Mater. Sci. Eng.-A **527**, 1 (2009).
56 K. L. Ngai, Phys. Rev. E **70**, 063501 (2004).
57 A. L. Greer, and F. Spaepen, Ann. NY Acad. Sci. **371**, 218 (1981).
58 P. Cao, M. P. Short, and S. Yip, Proc. Natl. Acad. Sci. **114**, 13631 (2017).
59 A. van den Beukel, and J. Sietsma, Acta Metall. Mater. **38**, 383 (1990).
60 Y. H. Liu, D. Wang, K. Nakajima, W. Zhang, A. Hirata, T. Nishi, A. Inoue, and M. W. Chen, Phys. Rev. Lett. **106**, 125504 (2011), arXiv: 1102.5598.
61 P. Zhang, J. J. Maldonis, Z. Liu, J. Schroers, and P. M. Voyles, Nat. Commun. **9**, 1129 (2018), arXiv: 1710.04791.
62 K. Tao, J. C. Qiao, Q. F. He, K. K. Song, and Y. Yang, Int. J. Mech. Sci. **201**, 106469 (2021).
63 M. R. J. Gibbs, J. E. Evetts, and J. A. Leake, J. Mater. Sci. **18**, 278 (1983).
64 W. Dmowski, T. Iwashita, C. P. Chuang, J. Almer, and T. Egami, Phys. Rev. Lett. **105**, 205502 (2010).
65 S. V. Khonik, A. V. Granato, D. M. Joncich, A. Pompe, and V. A. Khonik, Phys. Rev. Lett. **100**, 065501 (2008).
66 H. B. Ke, J. F. Zeng, C. T. Liu, and Y. Yang, J. Mater. Sci. Tech. **30**, 560 (2014).
67 J. Perez, Solid State Ion. **39**, 69 (1990).
68 A. V. Granato, and V. A. Khonik, Phys. Rev. Lett. **93**, 155502 (2004).
69 L. J. Santodonato, Y. Zhang, M. Feygenson, C. M. Parish, M. C. Gao, R. J. K. Weber, J. C. Neuefeind, Z. Tang, and P. K. Liaw, Nat. Commun. **6**, 5964 (2015).
70 L. A. Dissado, and R. M. Hill, Nature **279**, 685 (1979).
71 W. Jiao, B. A. Sun, P. Wen, H. Y. Bai, Q. P. Kong, and W. H. Wang, Appl. Phys. Lett. **103**, 081904 (2013).
72 C. Pei, R. Zhao, Y. Fang, S. Wu, Z. Cui, B. Sun, S. Lan, P. Luo, W. Wang, and T. Feng, J. Alloys Compd. **836**, 155506 (2020).
73 Z. Lu, W. H. Wang, and H. Y. Bai, Sci. China Mater. **58**, 98 (2015).
74 J. C. Qiao, Y. J. Wang, L. Z. Zhao, L. H. Dai, D. Crespo, J. M. Pelletier, L. M. Keer, and Y. Yao, Phys. Rev. B **94**, 104203 (2016).
75 G. P. Shrivastav, P. Chaudhuri, and J. Horbach, Phys. Rev. E **94**, 042605 (2016).
76 X. S. Yang, H. R. Zhai, H. H. Ruan, S. Q. Shi, and T. Y. Zhang, Int. J. Plast. **104**, 68 (2018).
77 G. Williams, and D. C. Watts, Trans. Faraday Soc. **66**, 80 (1970).
78 Z. Wang, B. A. Sun, H. Y. Bai, and W. H. Wang, Nat. Commun. **5**, 5823 (2014).
79 M. Atzmon, J. Appl. Phys. **123**, 065103 (2018).
80 A. S. Argon, J. Appl. Phys. **39**, 4080 (1968).
81 A. S. Argon, and H. Y. Kuo, J. Non-Cryst. Solids **37**, 241 (1980).
82 C. A. Schuh, and A. C. Lund, Nat. Mater. **2**, 449 (2003).
83 A. S. Argon, and L. T. Shi, Acta Metall. **31**, 499 (1983).
84 R. Bhowmick, R. Raghavan, K. Chattopadhyay, and U. Ramamurty, Acta Mater. **54**, 4221 (2006).
85 B. G. Yoo, Y. J. Kim, J. H. Oh, U. Ramamurty, and J. Jang, Scripta Mater. **61**, 951 (2009).